J Appl Electrochem (2017) 47:917–930
DOI 10.1007/s10800-017-1089-7

RESEARCH ARTICLE

Spectroscopic characterization and photoactivity of SiO_x-based films electrochemically grown on Cu surfaces

Agata Krywko-Cendrowska[1,2] · Laurent Marot[2] · Laetitia Philippe[3] · Marcin Strawski[1] · Ernst Meyer[2] · Marek Szklarczyk[1]

Received: 1 March 2017 / Accepted: 19 May 2017 / Published online: 26 May 2017

Abstract Electrodeposited SiO_x electrodes were shown to be photoactive and exhibit n- and p-type effects for electrodes placed in aqueous and organic solutions, respectively. As seen by Fourier transform infrared (FTIR) spectroscopy and X-ray photoelectron (XPS) spectroscopy, the mechanism of the electrodeposition included reactions with the used electrolyte as well as with traces of water as sources of oxygen and hydrogen. The lowest band gap energy (E_g) of the films of approximately 1.6 eV was observed for the film electrodeposited at −2.5 V in comparison to 1.9 eV for the films obtained at −2.25 and −2.75 V. The depth profiles of Si and O in the films were registered by XPS, secondary ion mass spectrometry (SIMS), and glow discharge optical emission spectroscopy (GD-OES), which showed that Si and O were relatively uniformly distributed across the entire layer of the film. The n-type photoactivity was associated with the evolution of oxygen from the aqueous solution, and the p-type was attributed to the reductive deterioration of the amorphous SiO_x deposit and simultaneous photodecomposition of the electrolyte.

✉ Agata Krywko-Cendrowska
agata.krywko@gmail.com

[1] Faculty of Chemistry, University of Warsaw, Pasteura 1, 02-093 Warsaw, Poland

[2] Department of Physics, University of Basel, Klingelbergstrasse 82, 4056 Basel, Switzerland

[3] EMPA, Swiss Laboratories for Materials Science and Technology, Feuerwerkstrasse 39, 3600 Thun, Switzerland

Graphical Abstract

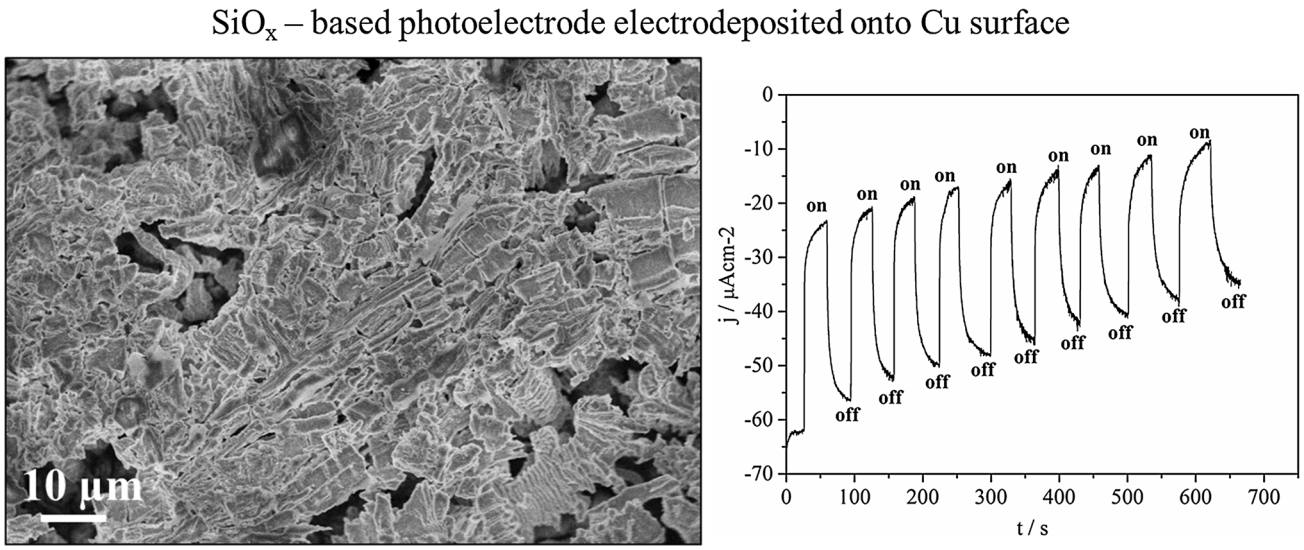

Keywords Silicon oxides · SiO_x · Electrodeposition · Photoactivity · Copper · XPS

1 Introduction

The search for cost-effective semiconductive layers suitable for photovoltaic and photogalvanic energy conversion has led to the proliferation of film production techniques. Silicon (Si) films are one of the most favorable substrates for photovoltaic applications due to silicon's properties and abundance [1–5]. Photogalvanic solar Si cells (wet solar cells) should be considered as an alternative to photovoltaic solar Si devices (dry solar cells). Their advantage is the possibility of generating not only electrical but also chemical energy in the form of hydrogen and oxygen in the water splitting process. The application of Si for this purpose has been known for several years [6–10]. The Si band gap (E_g) of approximately 1.1 eV ensures a high level of absorption of the solar spectrum, but elemental Si corrodes in aqueous solution, particularly in an anodic potential range. Si tends to form different types of oxides, from Si_2O, through SiO and Si_2O_3, to SiO_2 [11, 12]. These compounds exhibit E_g values in the range from 1.4 to 8.9 eV, which increase with the oxidation state of Si [13–17]. The oxides with E_g in the range of 1.4–2.5 eV (Si_2O, SiO, and Si_2O_3) should be considered as materials with a perfect band gap for the construction of photogalvanic cells. Due to their higher E_g values, they should also be much more resistant to photocorrosion in aqueous solutions than silicon itself.

Due to their properties, films containing SiO_x systems have already been gathering increasing interest over the last few years as candidates for light absorbing or emitting materials, e.g., in form of amorphous silicon oxide, a-SiO:H [18–20], Si nanoparticles embedded in a SiO_x matrix [21, 22], SiO_x/SiN_y multilayers [23], doped SiO_x/SiO_2 multilayers [24], silicon oxycarbide, and SiC_xO_y [25, 26].

Among the different methods of fabrication of Si-based materials, electrodeposition (ED) might be considered to be a low-energy consumption and low-cost alternative method to the standard industrial high-temperature methods. The ED of Si-based films started from attempts performed in water in 1854 [27]; however, the major observed problem was related to the often low or missed photoactivity of the fabricated Si films [2, 28]. While ED from organic solutions using an oxygen- and water-free regime is leading to Si deposits with purities as high as 98% [29], the addition of water to the system leads to a mixture of silicon oxides (SiO_x), and recently such SiO_x films instead of pure Si were proposed to face the issues coupled with the missing photoactivity of the electrodeposited Si films [13, 30].

In our previous work, we have observed n-type photoactivity in films formed from a mixture of SiO_x electrodeposited onto an Au surface both in aqueous [13] and organic [30] solutions. It was shown that the dependence of the photocurrent on the electrodeposition potential was volcano-like, with the strong maximum of the photocurrent observed for the film deposited at the middle potential value of the $SiHCl_3$ reduction wave [13, 30].

In this work, we present our results on the electrodeposition of amorphous SiO_x-based films onto a copper (Cu) surface and the investigation of their stoichiometry and photoactive properties using XPS, FTIR, SIMS, and GD-OES. Due to the much broader abundancy of Cu; its positive potential in the electrochemical series, like those of the noble metals; and its full recyclability, we believed that

Cu would be an interesting alternative to the scarce and costly noble substrates. In the long term, it could also open the possibility of using a CuO_x/SiO_x oxide-based p–n junction for tandem photogalvanic cells, where the CuO_x species could be used as the p-type component [31].

2 Experimental

2.1 Film preparation

A three-electrode system in a Teflon cell equipped with a quartz window was used for the ED of SiO_x films. The working electrode was polycrystalline 4 N Cu foil with a thickness of 0.125 mm. The working area was of circular shape with a 3 mm diameter if not stated otherwise. Platinum (Pt) and silver wire (Ag) were the counter and *quasi* reference electrodes, respectively. All potential values are given with respect to Ag. To improve the adhesion of the deposit to the substrate's surface and increase the working area of the Cu electrodes, a low-grained abrasive disc was used (CarbiMet S 600 [P1200], Buehler, USA). We expected that some amount of film would be deposited within the roughened surface while improving the adhesive properties of the lower parts of the films to the electrode.

All parts of the Teflon cell supposed to have contact with the electrolyte were cleaned with concentrated aqueous KOH (Chempur, pure p.a.) solution to remove the SiO_2 residue from the previous experiments. Then, they were thoroughly rinsed with water and dried under an air atmosphere. The electrodeposition was performed in 0.1 M tetrabutylammonium bromide (Fluka, puriss ≥99%, TBAB) dissolved in propylene carbonate (PC) (Sigma-Aldrich, anhydrous 99.7%). $SiHCl_3$ (Aldrich Chemistry, 98%) was used as the silicon source at a 0.5 M concentration. TBAB was dried under atmospheric pressure at 85 °C prior to use, and PC and $SiHCl_3$ were used as received. The water content of the prepared electrolyte was 920 ± 20 ppm. The choice of the chemicals used for the ED was justified in Reference [30]. Electrochemical experiments were carried out at an ambient temperature of 22 ± 2 °C under a constant argon (Ar) flow through the solution using either a μAutolab III potentiostat or an EG&G 263A potentiostat/galvanostat.

2.2 Photoelectrochemical measurements

After ED, the deposits were studied for their photoactivity either in 0.1 TBAB/PC or in 0.1 M $HClO_4$ aqueous solution. The 0.1 M $HClO_4$ was prepared by mixing the appropriate amounts of water (Milli-Q) and $HClO_4$ acid (Aldrich, 70%, A.C.S. Reagent). For illumination, a 1 kW ozone-free xenon lamp placed in a lamp housing (LSH 521, LOT ORIEL, Germany) was used. The intensity of the white light at the electrode's surface position measured with an IL 1700 light meter (International Light) equipped with a SEL033/F/W detector was 345 mW cm^{-2}. To filter out the long-wavelength radiation and to avoid excessive heating of the solution, a 10-cm-long water filter was placed between the cell and the light source. Prior to all other observations, the samples were rinsed with PC and dried under a weak Ar stream.

2.3 Morphology studies

The morphology of the deposits was monitored with secondary electron microscopy (SEM). The images were registered with a 5 keV electron beam energy and a low sample current value with a Hitachi S-4800 microscope.

2.4 Spectroscopy studies

Fourier transform infrared spectroscopy (FTIR), X-ray photoelectron spectroscopy (XPS), glow discharge optical emission spectroscopy (GD-OES), and secondary ion mass spectrometry (SIMS) were used to determine the chemical compositions of the deposits at the surface and at increasing depths.

FTIR spectra were recorded with an ALPHA Platinum ATR FTIR spectrometer equipped with a diamond crystal with a 2.4 refractive index (area approximately 2 mm^2) and OPUS/Mentor software (version 6.5).

XPS measurements were performed using a VG ESCALAB 210 system equipped with a monochromatized Al $K\alpha$ ($h\nu = 1486.6$ eV) radiation source, with a pass energy of 20 eV used for all narrow scan measurements. The photoemission spectra were recorded at normal emission with an overall resolution of approximately 0.6 eV. The energy positions of the spectra were calibrated with reference to the $4f_{7/2}$ level of a clean gold sample at a binding energy value of 84.0 eV. To avoid analysis of the native SiO_2 formed on the deposits after transporting them in air, the surfaces of the deposits were sputtered off with 2.5 keV Ar^+ for 90 min prior to measurements. Approximately 3 nm of the surface was sputtered as calculated using the ion current density measured with a Faraday cup (area 2 mm^2, measured ion current density 1.5×10^{-21} A nm^{-2}), which was placed at the sample position. The procedure is described in Reference [32]. XPS measurements were performed for three different sputtering times (0, 90, and 180 min), and after the first 90 min, the concentrations of Si and O did not depend on the sputtering time, indicating that the studied depth of the film exhibited elemental uniformity.

The spectra were charge corrected by shifting all of the energy values in a way that the second component of the

C1s signal appears at the literature value of 284.8 eV for the amorphous carbon [33] present in all of the deposits. Fitting of the data was performed using Doniach–Sunjic functions [34] after a Shirley background subtraction [35] with the help of UNIFIT 2011 software [36].

The band gap energies were determined based on narrow scan energy measurements between −2 and 5 eV, which allow probing of the valence electrons. Fitting of the Fermi edge was performed with the UNIFIT 2013 software. The detailed description of the procedure is given in Reference [30]. A convolution of Lorentzian and Gaussian line shapes was used to fit the individual peaks. After this, the intensities were estimated by calculating the integral of each peak. The atomic concentrations were then derived using Scofield sensitivity factors [37]. The total relative error on each concentration value was assumed to be 15% according to previous literature reports [38].

Ar plasma was used for GD-OES measurements, and spectra were recorded using the Imperial College vacuum UV Fourier transform spectrometer (FTS) and a free-standing Grimm-type GD source. The studied surface was 4 mm in diameter. The SIMS analysis was performed using a FIB/SEM-SIMS spectrometer (model C-TOF, TOF-WERK AG, Switzerland) using Ga ions as the sputtering source. In the case of the SIMS depth profiles, positive and negative measurements have been carried out under the same measurement conditions on two spots nearby each other on the Si layer to overlap the obtained depth profiles. The studied sample area was approximately 10 × 10 μm^2. For the needs of SIMS and GD-OES measurements, the diameter of the electrode's working area was increased to 7 mm. Due to application of the same electrodeposition procedure, the thickness of the deposits was significantly decreased.

3 Results and discussion

3.1 Electrodeposition of SiO_x films

In Fig. 1, the current–potential (*i–E*) dependencies for Cu electrodes placed in the basic electrolyte solution (a) and with the addition of $SiHCl_3$ as a silicon precursor (b) are presented. In the basic electrolyte, the current started to increase to approximately −2 V due to the reduction of H_2O traces present in the solution, and at approximately −2.6 V, the current increase could be identified with basic electrolyte and solvent decomposition [39].

When the Si precursor was added, in the range between approximately −1.2 and −2.2 V the observed current increased due to the reduction of hydrogen from HCl, which was the product of the reaction between the water traces present in the electrolyte and $SiHCl_3$ [30, 40]. The

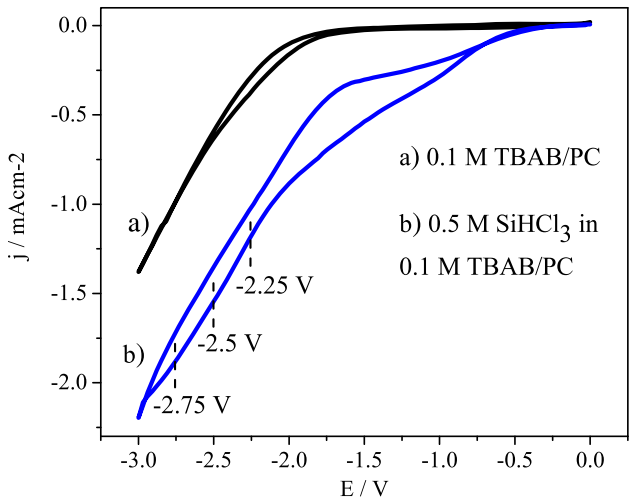

Fig. 1 *i–E* dependencies of the Cu electrode in 0.1 M TBAB/PC before (*a*) and after the addition of 0.5 M $SiHCl_3$ (*b*) registered at a scan rate of 50 mV/s. The chosen deposition potentials of −2.25, −2.5, and −2.75 V are marked with *dashed lines*

reduction of $SiHCl_3$ could be identified with the current wave appearing between −2.2 and −2.9 V [30, 40].

The electrodeposition potentials were chosen within this reduction wave and are marked in Fig. 1 by dashed lines (−2.25, −2.5, and −2.75 V). In Fig. 2, plots showing the current–time (*i–t*) dependencies for electrodeposition at these potentials are presented. For the curves registered at −2.25, −2.5, and −2.75 V, the calculated charge densities were 4.6, 8.1, and 10.7 C/cm^2, respectively. The linear increase in charge density with the deposition potential moving towards more cathodic values within the studied range implied a larger amount of deposit obtained. On the other hand, due to the electrolyte decomposition intensifying with the increase in the cathodic potential, the visible

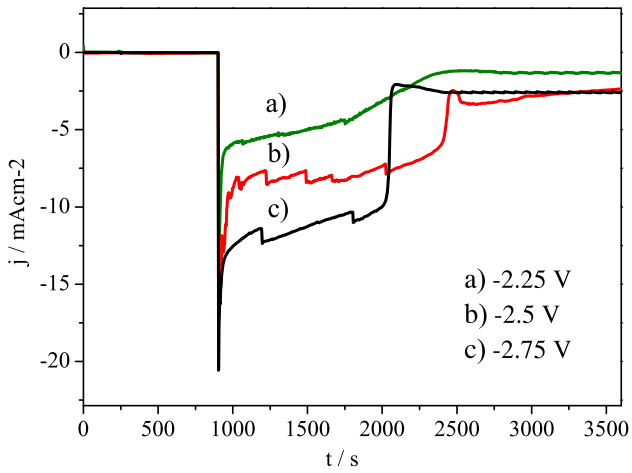

Fig. 2 *i–t* dependencies registered during the electrodeposition of silicon-based films on Cu at −2.25 (*a*), −2.5 (*b*), and −2.75 V (*c*) in 0.5 M $SiHCl_3$ in 0.1 M TBAB/PC

fluctuations observed in the curves were identified with gas bubble formation or desorption and in some cases also with the breaking of the film at more cathodic potentials, and thus, the calculated charge values should be treated with care.

3.2 Photoactivity of the SiO_x films

The results of the photoactivity tests obtained for the deposits both in organic (0.1 M TBAB/PC at −2 V) and aqueous (0.1 M $HClO_4$ at −0.3 V) solutions are presented in Fig. 3. The potential values for the photocurrent measurements were chosen within the stability ranges of both of the electrolytes used (organic and aqueous), deposits and Cu electrode in the case of its contact with the solution. For the ease of direct comparison of the influence of the substrate on the properties of the deposits, the potentials were the same as for the photoactive SiO_x deposits obtained on Au [13, 30].

Figure 3a shows an example of the *i–t* dependency registered under illumination in the aqueous solution. Based on this curve, the photocurrent was calculated as the difference between the current measured when the light was on and the dark current. The study of the photoactivity shows p- and n-type effects for electrodes placed in organic and water solutions, respectively (Fig. 3b, c). After the initial time (approximately 350 s), the photocurrent–time dependency (i_{ph}–*t*) in the organic electrolyte showed a two-fold increase in the photocurrent absolute value in case of the films obtained at −2.25 and −2.5 V. The p-type photocurrent observed in the organic solvent arose either from the reductive photodeterioration of the deposit or photodecomposition of the organic electrolyte (PC or TBAB). At this point, it should be mentioned that the p-type photocurrent could have also been enhanced by the presence of oxidized copper, which was due to the cracks in the deposit that could have been exposed to the electrolyte (this will be discussed in Sect. 3.4).

On the other hand, we believe that the n-type photocurrent registered in the $HClO_4$ aqueous solution was associated with the light-driven splitting of water molecules present in the electrolyte on the SiO_x surface, as previously observed for the films obtained on Au [13] (discussed later in detail). We have noticed that for the highest cathodic deposition potential studied here (−2.75 V), the photoactivity was not observed either in aqueous or organic solution. Additionally, the maximum value of the photocurrent was measured for the deposit obtained at a potential in the middle of the $SiHCl_3$ reduction wave (−2.5 V, Fig. 3b, c) with the same trend that was observed for SiO_x films electrodeposited onto Au surfaces at the same potential value [13, 30]. Similarly, the i_{ph}–*t* dependency for the deposits obtained on Cu placed in $HClO_4$ aqueous electrolyte showed a slow but steady decrease in the photocurrent value with time (Fig. 3c). On the contrary, the i_{ph}–*t* dependency for the deposits in TBAB/PC solution showed a slight increase until reaching a plateau, implying both of the photoactive films underwent a photoinduced modification upon being illuminated in an organic solution.

Compared to the deposits obtained on Au and tested for their photoactivity in the same conditions, the maximum photocurrent density of approximately 34 μAcm^{-2} was almost three-fold lower than the reported value (approximately 100 μAcm^{-2} [13]). On the other hand, while the photocurrent density in the organic solution remained at the

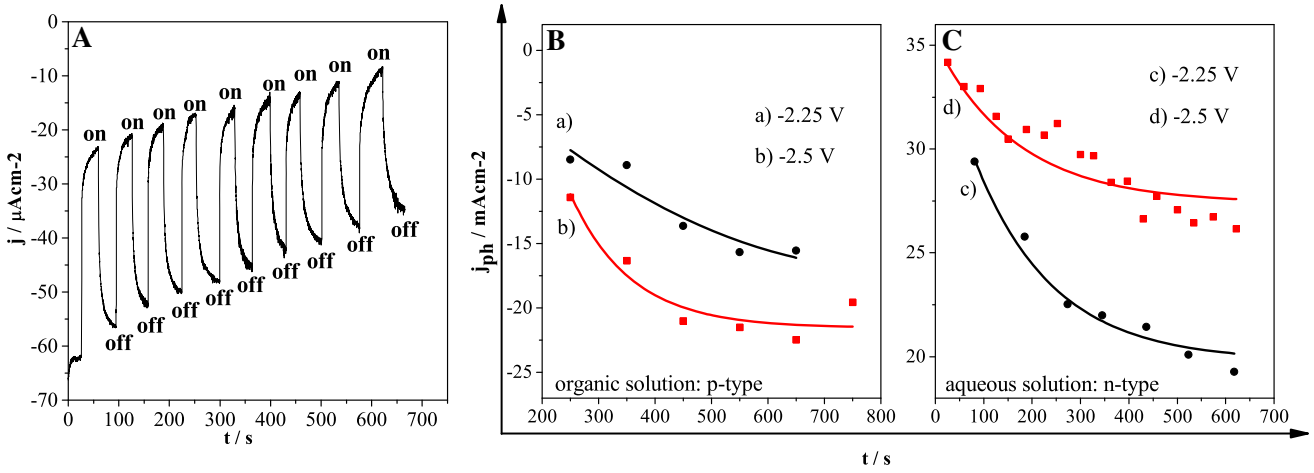

Fig. 3 **a** An example of the *i–t* dependency registered for the SiO_x deposit obtained on Cu at −2.5 V in 0.5 M $SiHCl_3$/0.1 M TBAB/PC under illumination in 0.1 M $HClO_4$ at −0.3 V. The descriptions "on" and "off" mean turning the illumination on and off. **b** p-type photocurrent values calculated for films at −2.25 (*a*) and −2.5 V (*b*) registered at −2 V in a 0.1 M TBAB/PC solution. **c** n-type photocurrent for films on Cu obtained at −2.25 (*c*) and −2.5 V (*d*) registered at −0.3 V in a 0.1 M aqueous $HClO_4$ solution

same level (approximately 20 μAcm^{-2}), it was of the p-type, meaning that in this case we observed the photoreduction reaction. The origin of this negative p-type photocurrent will be discussed in Sect. 3.7.

3.3 SEM imaging of electrodeposited SiO_x films

The morphology of the films was investigated before and after the photoelectrochemical measurements (Fig. 4). In the case of the film obtained at −2.25 V (Fig. 4a), the surface was not uniform with random microscale patterns visible on top, but the film seemed to be dense and compact. Since the intentionally made scratches were not revealed, we concluded that the electrode was covered uniformly over the area exposed to the electrodeposition. The surface of the deposit obtained at −2.5 V (Fig. 4b) showed a similarly patterned morphology, but some breaks in the film were observed. Their dimensions reached up to approximately 10 μm, and they were most likely caused by the simultaneously occurring decomposition of electrolyte during the ED process. As observed in the *i–E* dependency (Fig. 1), at −2.5 V the cathodic current registered for Cu in 0.1 M TBAB/PC was approximately 30% higher than that at −2.25 V, meaning that the decomposition of the electrolyte was more intense, which would explain the slight differences in the morphology of both of the deposits.

Further decreasing the ED potential led to a highly damaged surface with numerous cracks and holes (Fig. 4c, dark areas). Since at the highest cathodic ED potential the decomposition of the electrolyte was the most intense, it additionally confirmed the earlier conclusion. Figure 4d shows the surface of the deposit obtained at −2.5 V after photovoltaic measurements performed in 0.1 M $HClO_4$ aqueous solution. In comparison to the surface before being exposed to the illumination (Fig. 4b), it was damaged with numerous breaks (dark areas). Taking into account the decrease in the photocurrent value (Fig. 3c, curve d), we can conclude that the photodeterioration of the deposit occurred while working under illumination in aqueous solution.

This behavior was different than that observed for the SiO_x films electrodeposited onto the Au surface [13, 30], where the highest photoactivity was correlated to the most uniform film morphology. Here, we observed non-zero photocurrent for the most uniform morphology, but the highest photocurrent was still registered for the deposit

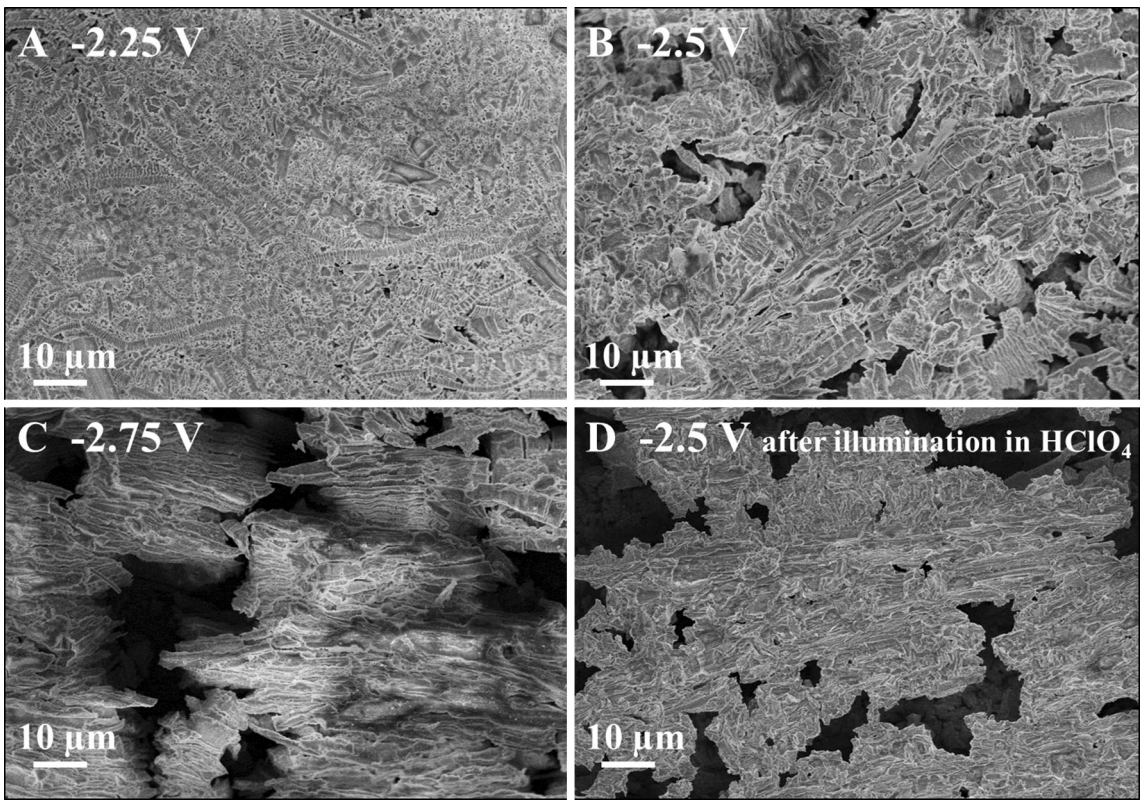

Fig. 4 Top view SEM images of the deposits obtained potentiostatically on a Cu electrode from 0.5 M $SiHCl_3$ at −2.25 (**a**), −2.5 (**b**), and −2.75 V (**c**) with 1 h of deposition time and of the deposit obtained at −2.5 V (**d**) after photoelectrochemical measurements in aqueous 0.1 M $HClO_4$

obtained at the potential value located in the middle of $SiHCl_3$ reduction wave (−2.5 V).

3.4 Spectroscopic characterization of electrodeposited SiO_x films

The FTIR spectra of the films deposited at −2.25, −2.5, and −2.75 V (Fig. 5) were of similar structure and contained bands corresponding to Si–H stretching modes in the range between 2100 and 2300 cm^{-1} [41–43], Si–O–Si stretching modes between 1000 and 1200 cm^{-1} [44–46], and Si–H rocking modes between 650 and 800 cm^{-1} [47]. While the intensity of the signals arising from the Si–H bond was independent of the deposition potential, the Si–O band intensity was slightly higher for the film obtained at −2.5 V, i.e., the most photoactive film. The weak bands between 945 and 990 cm^{-1} corresponded to the stretching mode of the Si–O–C bond [41]. Its asymmetric stretching mode occurred in the same range as the band arising from the Si–O–Si bond stretching (1000–1200 cm^{-1}) [44].

The XPS analysis showed the presence of Si, O, and C for all of the films and Cu for the films deposited at −2.25 and −2.5 V. Si2p, C1s, and $Cu2p_{3/2}$ core level spectra registered for the films obtained on Cu at −2.25, −2.5, and −2.75 V are presented in Fig. 6. After the deconvolution, the Si2p spectra of the films obtained at −2.5 and −2.75 V showed two different components corresponding to SiO (at 101.3 eV) [48–50] and Si_2O_3 (at 103.5 and 103.6 eV) [48–50]. No elemental Si was detected.

Taking into account only the Si and O concentrations, it was possible to determine the overall stoichiometry of the SiO_x species in films. The calculated atomic concentrations for Si and O were approximately 40 and 60 at.% for the films deposited at −2.5 and −2.75 V, respectively, resulting in a total Si:O ratio of 0.7 (Table 1).

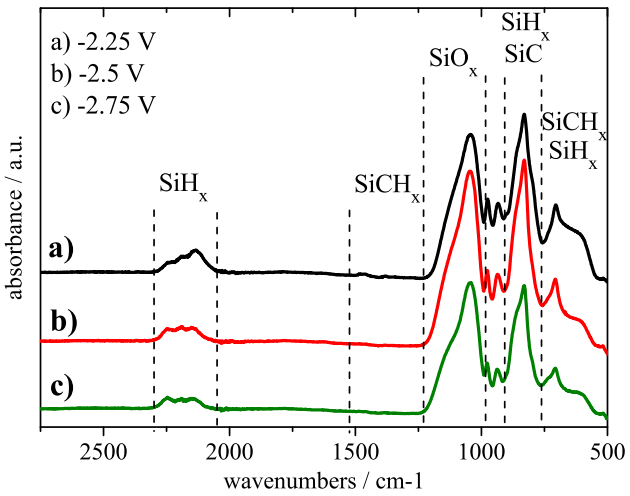

Fig. 5 FTIR spectra of Si-based films obtained potentiostatically on Cu electrodes from 0.5 M $SiHCl_3$ at −2.25 (*a*), −2.5 (*b*), and −2.75 V (*c*) with 1 h of deposition time. The spectra are presented in vertical shift

In the spectrum of the film obtained at −2.25 V, the presence of SiO was observed as well (at 101.4 eV, 13.7 at.%), and in addition to this, the Si_2O_3 and Si_2O species were also deconvoluted (102.9 eV, 23.7 at.% and at 99.8 eV, 9.6 at.%, respectively) [48–50]. The calculated total Si:O ratio for this film was 0.9 and was the highest out of the three values.

The signal from Si_2O disappeared with a decrease of the electrodeposition potential and simultaneous increase of the SiO_2 concentration.

The deconvolution of the C1 s core level spectra (Fig. 6) showed two components, one corresponding to amorphous carbon at 248.8 eV, present due to the decomposition of the electrolyte during the deposition. Due to the overlaying of the binding energy ranges for Si–C and Si–O bonds in the Si2p spectrum and the low concentration of Si atoms bonded to C in comparison to those bonded to O, it was not possible to deconvolute this signal in the Si2p spectrum. On the other hand, in the C1s spectrum, the signal corresponding to Si–C species was deconvoluted at 282.3 eV [51, 52], similar as for the SiO_x films on Au reported already in our previous paper [30]. The determined concentration of C for both deposits was approximately 4 at.%.

For ED potentials of −2.25 and −2.5 V, the trace amounts of Cu atoms were detected (Fig. 6). For the first film, the BE value was 934.2 eV and corresponded to CuO [50] (<0.5 at.%). For the latter deposit, the peak was assigned to Cu_2O [50] (933 eV, 1.6 at.%). An explanation for the presence of a Cu signal could be the breaking of the films after drying. Taking into account the low content of water in the electrolyte, the kinetics of Cu corrosion caused by water, and the thermodynamic stability of Cu in the conditions of the experiments performed [53–55], the presence of oxidized copper species could only be due to the growth of the native copper oxide in air. On the other hand, due to the low growth rate of the native CuO_x (approximately 3.3 nm in 48 h, mixed Cu_2O and CuO oxide forms [56]), the resulting thickness of the oxide (after a max of approximately 3 min before placement in the electrolyte) would not be enough to form p-n CuO_x/SiO_x junctions or to contribute to the photoactivity of the system and could be neglected in further discussion.

The E_g values determined by XPS were 1.9, 1.6, and 1.9 eV for films deposited at −2.25, −2.5, and −2.75 V, respectively. All three E_g values were within the range of E_g values corresponding to either lower SiO_x (for $0.8 < x < 1$ [16, 57]) or SiO_xC_y species, the band gap of which would depend on the C content, from 1.21 to 1.75 eV in a SiO_x-rich structure [58], to approximately 1.9 eV in SiO_x containing 6–8 at.% C [25, 59–62]. In this

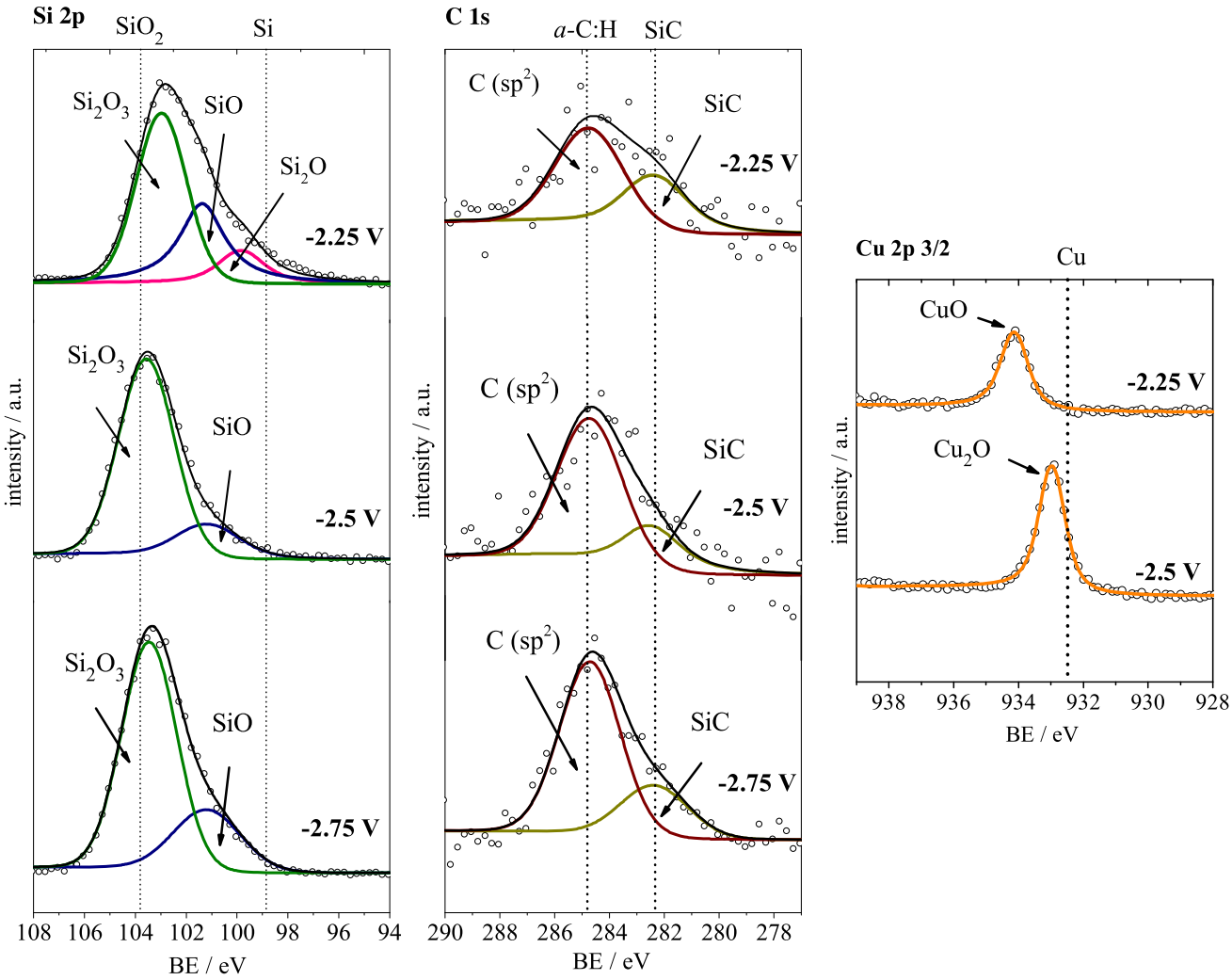

Fig. 6 XPS Si2p, C1s, and Cu2p core level spectra of the of SiO_x films deposited potentiostatically on Cu from 0.5 M $SiHCl_3$ at −2.25, −2.5, and −2.75 V with 1 h deposition time. The presence of Cu was not observed for the film deposited at −2.75 V; the *colored lines* are the different components; the *open circles* are the measurement points; and the *solid black line* is the fit sum of the components

Table 1 Dependence of the Si and O concentration ratio on the deposition potential of the Si-based films on Cu from 0.5 M $SiHCl_3$ with 1 h of deposition time determined by XPS; the concentrations were determined after 90 min of Ar^+ sputtering

	−2.25 V	−2.5 V	−2.75 V
Si:H (at.%)	–	–	–
Si_2O (at.%)	9.6	–	–
SiO (at.%)	13.7	7.4	10.3
Si_2O_3 (at.%)	23.7	32.7	30.5
SiO_2 (at.%)		–	–
∑Si (at.%)	47	40.1	40.8
∑O (at.%)	53	59.9	59.2
Total Si/O ratio	0.9	0.7	0.7

case, the difference of 2 at.% would be negligible, taking into account the standard error of the measurement. The value calculated for the two latter deposits could also correspond to CuO_x [62, 63]. However, as already explained, the thickness of the CuO_x was not enough to form a semiconductive layer.

3.5 Mechanism of the electrodeposition

As already reported previously [13, 30], the SiO_x species could be produced via the electrochemical reduction of $SiHCl_3$ in TBAB/PC solution with a low H_2O content according to the following reaction:

$$SiHCl_3 + xH_2O + xe^- \rightarrow SiO_x + (x + 0.5)H_2\uparrow + 3Cl^- \quad (1)$$

which would also be the case for the films synthesized in this work. The Si:O ratio measured by XPS (Fig. 6, Table 1) showed that with a decrease of the ED potential, the concentration of oxygen-containing species increased.

This increase in the oxygen concentration occurred with a decrease in the deposition potential from −2.25 to −2.5 V; thus, the higher concentration of the more oxidized SiO_x species can be explained by the simultaneous cathodic decomposition of PC via carbonate radicals, which would act as a source of oxygen species [13, 30, 64]. This would cause the oxidation of the SiO_x already produced according to Reaction 1 and an overall increase in the oxygen concentration in the films according to the following processes:

$$PC + 1e^- \rightarrow (C_3H_6)CO_3^{-\cdot} \quad (2)$$

followed by

$$\cdot(C_3H_6)\,CO_3^- + SiO_x^{dep} \rightarrow C_3H_6\uparrow + CO_2\uparrow + SiO_{x+0.5} \quad (3)$$

Since the further decrease of the deposition potential did not lead to an increase of the oxygen concentration, we could state that the decomposition of PC was occurring steadily in this potential range and would not further affect the stoichiometry of the films.

Similarly as for the deposits obtained on Au in our previous work, the supporting electrolyte, TBAB, was decomposing throughout the entire potential range studied here. The decomposition of TBAB typically occurs through radicals, and since radicals are not stable and very reactive, they were the source of Si–C bonds, which would explain the presence of the low amount of carbon incorporated into the films. In addition to this, another source of the carbon content could be the low amount of silanols formed in the reaction between $SiHCl_3$ and the H_2O content present in the electrolyte [30, 40]:

$$R_3SiCl + H_2O \rightarrow R_3SiOH + HCl. \quad (4)$$

The silanols formed due to their typical tendency to condense, and the formation of the Si–O–Si linkages [65] could form the bonds to the deposits and be the source of O–Si–C photoactive centers contributing to the photoactivity of the films [25].

3.6 SIMS and GD-OES depth profiles

The results of the SIMS profiling are presented in Fig. 7. Figure 7a shows the surface of the deposit with the bright square-shaped area of 10 × 10 μm^2, for which the SIMS measurements were performed. Figure 7b shows the surface distribution of Si (upper image) and its distribution throughout the depth of the deposit (bottom image). It could be observed that although the Si distribution was relatively uniform, brighter areas with higher concentrations of Si appeared. Comparing the top view SEM picture with the distribution of Si, it could also be observed that the areas of higher Si concentration were in the places where the surface exhibited some non-uniformities, which indicated the topography effect. In Fig. 7c, a similar trend was observed as well. The cleavage-shaped brighter areas of higher O concentration also appeared under the non-uniformities visible on top of the deposit, meaning that Si and O were present throughout all of the studied layers with a relatively uniform distribution. In comparison, the oxygen was present across the entire layer, but its concentration was higher close to the surface, which was identified with the native SiO_2 on top of the deposit (the XPS measurements were performed after sputtering off this native layer).

The GD-OES depth profile of the layer deposited on Cu from 0.5 M $SiHCl_3$ at −2.5 V was registered after calibration of the spectrometer on crystalline Si (*c*-Si) to estimate its thickness (Fig. 8a). Since the surface of the electrode prior to deposition was intentionally roughened to improve the adhesive properties of the film and enlarge the working area of the electrode for the ED process, we expected that a high amount of the film would be deposited in the scratches as well. Figure 8b is the zoomed-in image of Fig. 8a, and it shows the estimated thickness range where the lines corresponding to Si and Cu signals crossed.

The concentration of Si within the first 10 nm was constant (Fig. 8d), and such behavior was observed by SIMS as well (Fig. 8b). After approximately 10 nm, the line corresponding to Si dropped while the Cu signal followed a fast increase. We assumed that this was the bottom of the bulk SiO_x deposit on Cu, and furthermore, the observed Si was within the roughened thickness of Cu. From approximately 20 nm onward, the line arising from Si followed a slow decay, which is characteristic for the films obtained on rough substrates, until approximately 0.35 μm, where it reached 0 at.%.

The normalized dependency of the atomic concentrations of the elements of interest on the sputtering time is shown in Fig. 8c, and the same zoomed-in area where the Si and Cu signals crossed is presented in Fig. 8d. The calculated Si-to-H atomic concentration ratio in the depth of the deposits was determined as being close to 1. This was not in agreement with the XPS results, where no Si:H was observed on the sputtered photoactive surface.

3.7 Discussion

The observed photocurrent, p-type for the SiO_x-based film placed in organic solution (Fig. 3b) and n-type for the SiO_x-based film placed in the aqueous solution (Fig. 2c), corresponded to the photoreduction and photooxidation reactions, respectively.

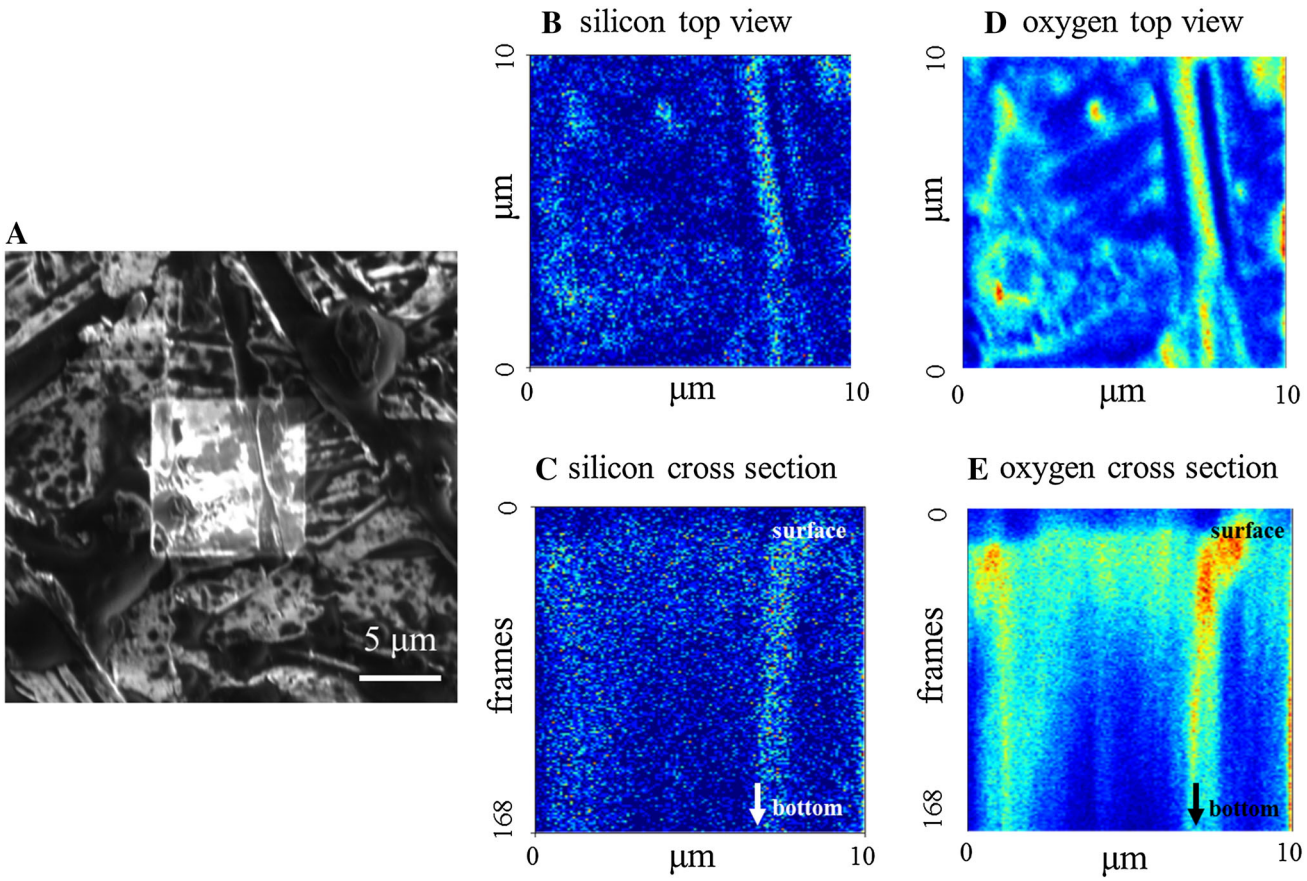

Fig. 7 A. SEM top view of the deposit obtained on Cu at −2.5 V from 0.5 M $SiHCl_3$. **a** The brighter area with a size of 10 × 10 μm^2 was analyzed by SIMS for the distribution of silicon; **b** surface; **c** cross section and distribution of oxygen; **d** surface; **e** cross section with the brighter places indicating a higher concentration of the element of interest

Figure 9 shows the FTIR spectra registered for the film synthesized at −2.25 V before (curve a) and after photogalvanic measurements performed in organic (b) and aqueous solutions (c).

The illumination of the deposits in the organic solution yielded p-type photocurrent ranging from ca 20 to 35 µA/cm^2 for the deposits obtained at −2.25 and −2.5 V, respectively. In both cases, the current followed the same steady increase until reaching a plateau, implying a light-induced change in the films. In comparison to the spectrum of the film from before the illumination, its spectrum after the illumination in the organic solution contained new bands arising from the C=O species and Si–CH_x species (approximately 1800 cm^{-1} [30, 41]) appearing due to the photodecomposition of the electrolyte and incorporation of its product into the films. Since hydrogen was the product of this photodecomposition as well, it was presumably reduced at the potential of the experiment (−2 V) and was built into the films, which could be confirmed by the increase in the intensity of the bands correlated to the Si–H species (Fig. 9, range 2250–2500 cm^{-1}). All of these photoinduced changes were of the reductive type, and thus, they slightly increased the photocurrent value registered in time (Fig. 3b) by increasing the concentration of the photoactive species and reducing the Si oxidation state.

After the illumination in $HClO_4$ solution, the intensity of the bands corresponding to Si–H significantly decreased (Fig. 9, line c), meaning that the low amount of the H-containing Si species present underwent photodecomposition. As the intensities of the bands corresponding to Si–O species did not change, it could be stated that SiO_x did not photodecompose and was acting as the photoactive material. On the other hand, through the incorporation of carbon within the SiO_x deposit, a low percentage of photoactive O–Si–C centers was created, which could have stabilized the photocurrent.

SiO_x species are well-known for their n-type behavior in [66], and we can assume the same photoactive nature of SiO_x reported here. The results on the photoactivity of our SiO_x films in aqueous solution (Fig. 3c) showed the highest n-type photoactivity of the films for the −2.5 V deposition potential, indicating that at this potential value deposits contained the highest concentration of SiO_x species. In aqueous solution, the slow photocurrent decrease was

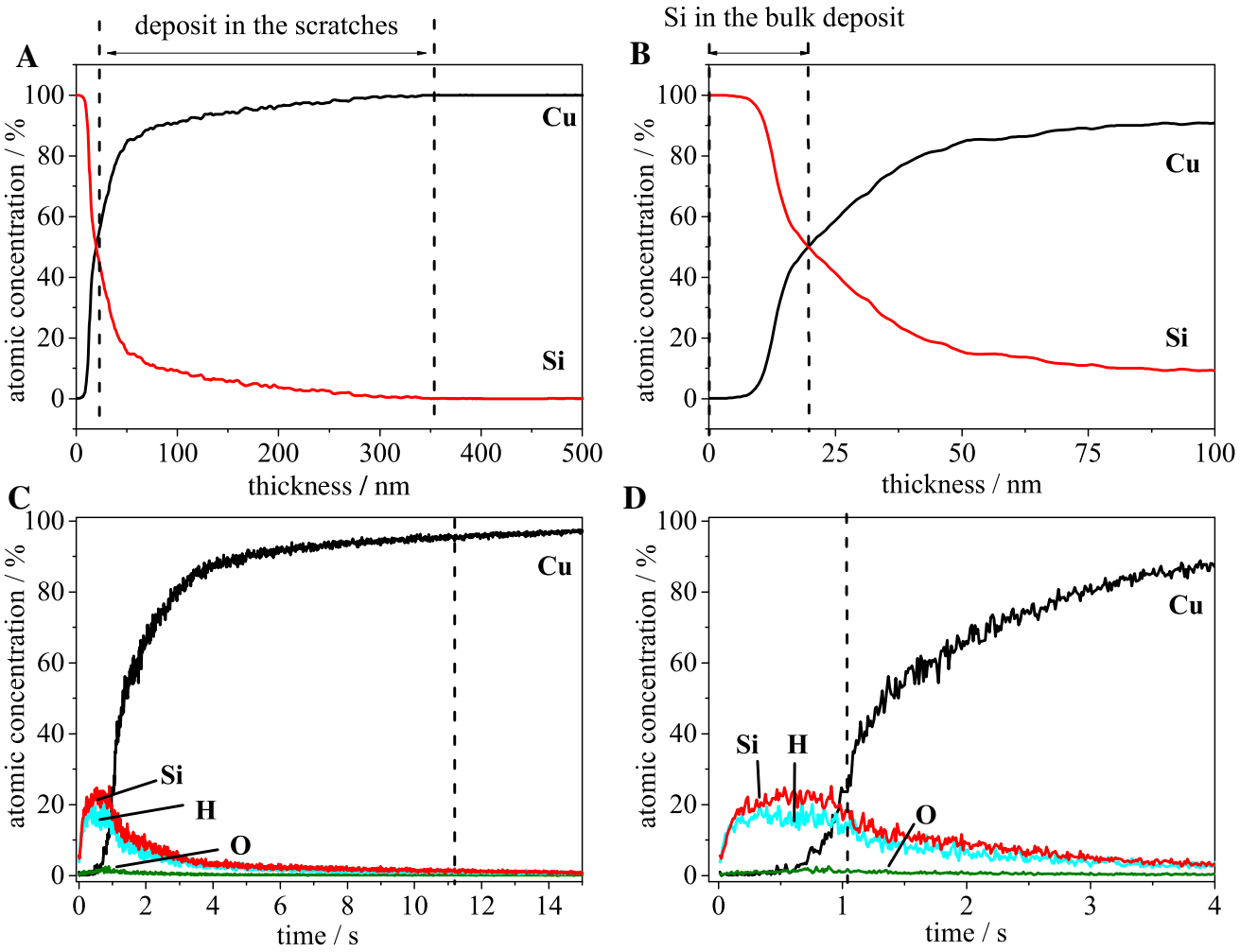

Fig. 8 **a** Dependency of the Si concentration of the deposit obtained on Cu from 0.5 M $SiHCl_3$ at −2.5 V obtained by GD-OES after calibration of the sputtering rate on crystalline Si. **b** Zoomed-in image of the region with the highest concentration of Si. **c** Depth profile of the same deposit with other elements of interest taken into account. **d** Zoomed-in image of the same range as in (**b**)

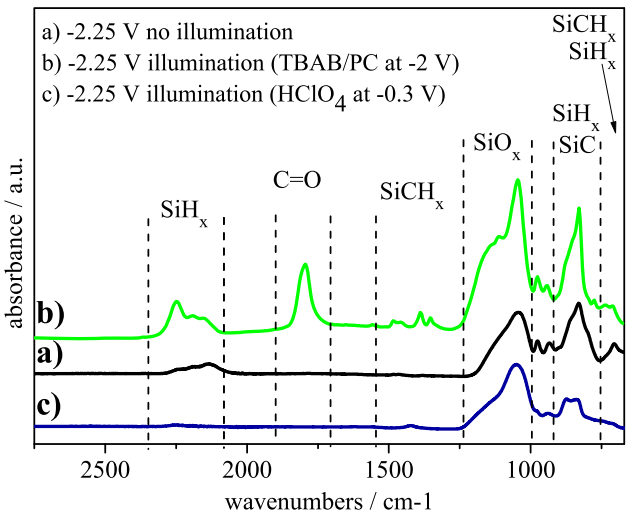

Fig. 9 FTIR spectra of the deposit obtained at −2.25 V before (*a*) and after illumination in 0.1 M TBAB/PC at −2 V (*b*) and in aqueous 0.1 M $HClO_4$ at −0.3 V (*c*)

related to the decrease in the concentration of photoactive species detected by FTIR studies (Fig. 9 curve c, the ranges of 800–450 and 1200–1000 cm^{-1}, respectively). Furthermore, it should be noted that although the intensity of the band corresponding to the Si–H bonds decreased to zero, the photocurrent value kept steadily decreasing until reaching a plateau, meaning that the main species responsible for the photoactivity was SiO_x. The steady decrease of the photoresponse could be associated with the slow oxidation of the film (Fig. 9) occurring due to the evolution of oxygen [30].

In comparison to the films previously obtained on Au, in which the photoactivity in aqueous solution was based on minimally oxidized SiO_x and Si:H, the response of the system while illuminated was fast and stable, although the photocurrent value itself was approximately three times smaller than the one reported for H_2O oxidation [13]. Since the SiO_x deposited here was more oxidized than that on Au,

it could be stated that the higher efficiency of H_2O oxidation was correlated to the lower Si oxidation state. We concluded that the photocurrent was stabilized due to the low carbon content, and we correlated it to the presence of luminescent O–Si–C centers reported for the oxycarbides, SiO_xC_y, having approximately 8–6 at.% of C [59, 60], with the C content acting as a deep-embedded defect in the SiO_x matrix and affecting its photoactivity.

The observed surface morphology changes (Fig. 4b, d) could be explained by the possible oxidation of the film by evolving oxygen and the formation of a SiO_2 layer [30]. The lowest observed band gap was determined for the film obtained at −2.5 V, and this value actually corresponded to minimally carbon-doped silicon oxides, for which E_g was changing with the amount of C [57–61]. With the low concentration of carbon in the films, it can be concluded that although such species were formed, the main component responsible for the photoactivity of the films was still SiO_x [57], with the O–Si–C centers acting as the stabilizer of the photocurrent [59, 60] in aqueous solution.

There were some inconsistencies between the presented FTIR (Fig. 5) and XPS results (Fig. 6), which did not show the presence of Si–H_x species. This could be explained by the probing depths of both techniques. In the FTIR, the wavelength ranges of interest were 800–450 and 1200–1000 cm^{-1}, and thus, the penetration of the probing beam could be from 12 to 22 μm and 8.3 to 10 μm, respectively, meaning that the whole film was probed. In case of the XPS signal, the escape depth was much smaller, and in the case of Si-based materials, it was approximately 1–2.2 nm for Si and approximately 2.1 nm for SiO_2 [67, 68]. Thus, after sputtering off the native SiO_2 layer, the XPS signal was collected from a much thinner layer, within which the Si–H_x species were not present or present at a very low concentration and which was actually working under illumination. Also, the illumination could cause the Si–H bond breaking and moving of the H radicals to the surface (Staebler–Wronski effect), followed by their immediate oxidization there.

For the film obtained at −2.75 V, no photocurrent was observed either in aqueous or organic solution, and the reasons for this outcome could be either morphological or chemical. For example, due to the non-uniform morphology of the film (Fig. 4c), the well-developed depletion layer could be not formed, similar to the deposits obtained on Au [30]. On the other hand, a decrease of the electrodeposition potential led to a thicker film (higher deposition charge), i.e., an increase in the more oxidized SiO_x-containing film thickness was observed, which increased the resistivity of the film and resulted in the lack of contact of the copper substrate with the solution.

4 Conclusion

To conclude, in this work, we described the electrosynthesis of photoactive SiO_x deposited on Cu. Its chemical composition has been determined by FTIR and XPS techniques and explained by the electrodeposition reaction, including the contribution of the electrolyte and traces of water, which were the sources of oxygen, a low content of carbon and hydrogen. The morphologies of the films were studied by SEM, and they were shown to be dependent on the deposition potential. The registered SIMS and GD-OES depth profiles have shown the Si, O, and H distributions in the bulk of the synthesized film and that a significant amount of the film was deposited in the non-uniformities of the prepared Cu surface. The lowest band gap energy of the fabricated films was approximately 1.55 eV, and it was observed for the film deposited at −2.5 V. Since it did not correspond to any of the species in the film, it was proposed that a small amount carbon incorporated into the deposits caused the formation of silicon oxycarbides, which acted as a stabilizer of the photocurrent in the aqueous solution. Although the registered photocurrent density value was lower than those previously reported for the films on Au, the use of Cu substrate would be an economic alternative to the noble metal electrodes, and if accompanied by CuO_x of a controlled thickness, it could open the possibility to apply a p–n CuO_x/SiO_y junction for the construction of a cheap and efficient photogalvanic solar cell.

Acknowledgements The authors acknowledge the Foundation of Polish Science MPD Program cofinanced by the EU European Regional Development Fund, Swiss Federal Office of Energy, and Swiss Federal Office for Education and Science for their financial support. This work was also supported by the Swiss National Foundation (SNF), Swiss Nanoscience Institute (SNI), and National Centre of Competence in Research on Nanoscale Science. We would also like to express our thanks to Prof. Wolfgang Meier for making the ATR FTIR spectrometer available to us, Mr. Daniel Mathys for the SEM imaging, and Mr. Damian Frey for the GD-OES measurements presented in this work.

References

1. Rao GM, Elwell D, Feigelson RS (1982) Characterization of electrodeposited silicon on graphite. Sol Energy Mater 7:15–21
2. Pudasaini PR, Ayon AA (2012) High efficiency nanotextured silicon solar cells. Opt Commun 285:4211–4214
3. Yoo J, Yu G, Yi J (2011) Large-area multicrystalline silicon solar cell fabrication using reactive ion etching (RIE). Sol Energy Mater Sol Cells 95:2–6
4. Bugnon G, Parascandolo G, Söderström T, Cuony P, Despeisse M, Hänni S, Holovský J, Meillaud F, Ballif C (2012) A new view of microcrystalline silicon: the role of plasma processing in achieving a dense and stable absorber material for photovoltaic applications. Adv Funct Mater 22:3665–3671
5. Hamashita D, Miyajima S, Konagai M (2012) Preparation of Al-doped hydrogenated nanocrystalline cubic silicon carbide by

VHF-PECVD for heterojunction emitter of n-type crystalline silicon solar cells. Sol Energy Mater Sol Cells 107:46–50
6. Noda M (1982) Photo-assisted electrolysis of water by Si photoelectrodes. Int J Hydrog Energy 7:311–320
7. Szklarczyk M, Bockris JOM (1983) Photoelectrocatalysis on silicon in solar light. Appl Phys Lett 42:1035–1036
8. Gissler W, McEvoy AJ (1984) Photoelectrochemical effects on p-silicon of ruthenium dioxide thin films. Sol Energy Mater 10:309–316
9. Kenney MJ, Gong M, Li Y, Wu JZ, Feng J, Lanza M, Dai H (2013) High-performance silicon photoanodes passivated with ultrathin nickel films for water oxidation. Science 342:836–840
10. Hull R (1999) Properties of crystalline silicon. INSPEC, Stevenage
11. Dearnaley G, Morgan DV, Stoneham AM (1970) A model for filament growth and switching in amorphous oxide films. J Non-Cryst Solids 4:593–612
12. Priestley EB, Call PJ (1980) Deposition and characterization of thin SiO_x films. Thin Solid Films 69:39–52
13. Krywko-Cendrowska A, Strawski M, Szklarczyk M (2013) Low temperature electrodeposition of SiO_x films photoactive in water solution. Electrochim Acta 108:112–117
14. Thøgersen A, Selj JH, Marstein ES (2012) Oxidation effects on graded porous silicon anti-reflection coatings. J Electrochem Soc 159:D276–D281
15. Weinberg ZA, Rubloff GW (1978) The Physics of SiO_2 and its interfaces. Pergamon, New York
16. Tomozeiu N (2011) Silicon oxide (SiO_x, $0 < x < 2$): a challenging material for optoelectronics. In: Predeep P (ed) Optoelectronics-materials and techniques. Intech, pp 55–99. doi: 10.5772/20156
17. Barranco A, Yubero F, Espinos JP, Groening P, Gonzalez-Elipe AR (2005) Electronic state characterization of SiO_x thin films prepared by evaporation. J Appl Phys 97:113714
18. Walder C, Kellermann M, Wendler E, Rensberg J, von Maydell K, Agert C (2015) Comparison of silicon oxide and silicon carbide absorber materials in silicon thin-film solar cells. EPJ Photovolt 6:65302
19. Haga K, Yamamoto K, Kumano M (1990) Optical properties of plasma-deposited silicon-oxygen alloy films. Jpn J Appl Phys 29:636–639
20. Fujikake S, Ohta H, Asano A, Ichikawa Y, Sakai H (1992) High quality a-SiO: H films and their application to a-Si solar cells. Mater Res Soc Symp Proc 258:875
21. Pavesi L, Dal Negro L, Mazzoleni C, Franzo G, Priolo F (2000) Optical gain in silicon nanocrystals. Nature 480:440–444
22. Nayfeh M, Rao S, Barry N, Therrien J, Belomoin G, Smith A, Chaieb S (2002) Observation of laser oscillation in aggregates of ultrasmall silicon nanoparticles. Appl Phys Lett 80:121–123
23. Nalini RP, Khomenkova L, Debieu O, Cardin J, Dufour C, Carrada M, Gourbilleau F (2012) SiO_x/SiN_y multilayers for photovoltaic and photonic applications. Nanoscale Res Lett 7:124
24. Gourbilleau F, Dufour C, Madelon R, Rizk R (2007) Effects of Si nanocluster size and carrier Er interaction distance on the efficiency of energy transfer. J Lumin 126:581–589
25. Nikas V, Gallis S, Huang M, Kaloyeros AE, Nguyen APD, Stesmans A, Afanas'ev VV (2014) The origin of white luminescence from silicon oxycarbide thin films. Appl Phys Lett 104:061906
26. Wang M, Xia Y, Wang X, Xiao Y, Liu R, Wu Q, Qiu B, Metwalli E, Xia S, Yao Y, Chen G, Liu Y, Liu Z, Meng Q, Yang Z, Sun LD, Yan CH, Müller-Buschbaum P, Pan J, Cheng YJ (2016) Silicon oxycarbide/carbon nanohybrids with tiny silicon oxycarbide particles embedded in free carbon matrix based on photoactive dental methacrylates. ACS Appl Mater Interfaces 8:13982–13992
27. Gore C (1854) Electro-deposition of aluminium and silicium. Philos Mag 7:227–228
28. Nicholson JP (2005) Electrodeposition of silicon from nonaqueous solvents. J Elecrochem Soc 152:C795–C802
29. Bechelany M, Elias J, Brodard P, Michler J, Philippe L (2012) Electrodeposition of amorphous silicon in non-oxygenated organic solvent. Thin Solid Films 520:1895–1901
30. Krywko-Cendrowska A, Marot L, Strawski M, Steiner R, Meyer E (2016) Electrodeposition and characterization of SiO_x films photoactive in organic solution. J Electrochem Soc 163:D100–D106
31. Paracchino A, Brauer JC, Moser JE, Thimsen E, Graetzel M (2012) Synthesis and characterization of high-photoactivity electrodeposited Cu_2O solar absorber by photoelectrochemistry and ultrafast spectroscopy. J Phys Chem C 116:7341–7350
32. Useful Information and Facts about the Practice of Sputtering, SPECS Surface Nano Analysis GmbH. http://www.specs.de/cms/upload/PDFs/IQE11-35/sputter-info.pdf
33. Pellison-Schecker A, Hug HJ, Patscheider J (2012) Charge referencing issues in XPS of insulators as evidenced in the case of Al-Si-N thin films. Surf Interace Anal 44:29–36
34. Doniach S, Sunjic M (1970) Many-electron singularity in X-ray photoemission and X-ray line spectra from metals. J Phys C 3:285–291
35. Shirley DA (1972) High-resolution X-ray photoemission spectrum of the valence bands of gold. Phys Rev B 5:4709–4714
36. Hesse R, Chasse T, Szargan R (1999) Peak shape analysis of core level photoelectron spectra using UNIFIT for WINDOWS. Fresen J Anal Chem 365:48–54
37. Scofield JH (1976) Hartree-Slater subshell photoionization cross-sections at 1254 and 1487 eV. J Electron Spectrosc Relat Phenom 8:129–137
38. Tougaard S (1998) Accuracy of the non-destructive surface nanostructure quantification technique based on analysis of the XPS or AES peak shape. Surf Interface Anal 26:249–269
39. Izutsu K (2002) Electrochemistry in nonaqueous solutions. Wiley, ISBN: 3-527-60065-5
40. Agrawal AK, Austin AE (1981) Electrodeposition of silicon from solutions of silicon halides in aprotic solvents. J Electrochem Soc 128:2292–2296
41. Socrates G (2004) Infrared and Raman characteristic group frequencies, 3rd edn. Wiley, Chichester
42. Brodsky MH, Cardona M, Cuomo JJ (1977) Infrared and Raman spectra of the silicon-hydrogen bonds in amorphous silicon prepared by glow discharge and sputtering. Phys Rev B 16:3556–3571
43. Deschaines T, Hodkiewicz J, Henson P (2009) Characterization of amorphous and microcrystalline silicon using Raman spectroscopy. Technical Note 51735, Thermo Fischer Scientific, Madison, WI, USA. https://tools.thermofisher.com/content/sfs/brochures/D16998~.pdf
44. Kingma KJ, Hemley RJ (1994) Raman spectroscopic study of microcrystalline silica. Am Miner 79:269–273
45. Katharria YS, Kumar S, Choudhary RJ, Prakash R, Singh F, Lalla NP, Phase DM, Kanjilal D (2008) Pulsed laser deposition of SiC thin films at medium substrate temperatures. Thin Solid Films 516:6083–6087
46. Bennet CJ, Sillars D, Osamura Y, Kaiser RI (2005) Infrared spectroscopic identification of the methylsilylidyne ($SiCH_3$, X^2A'') and the silenyl (H_2CSiH, X^2A') radicals in methane-silane matrices. Chem Phys Lett 404:327–335
47. Kroll U, Meier J, Shah A, Mikhailov S, Weber J (1996) Hydrogen in amorphous and microcrystalline silicon films prepared by hydrogen dilution. J Appl Phys 80:4971–4975
48. Texeira F, Berjoan R, Peraudeau G, Perarnaru D (2005) Solar preparation of SiO_x ($x \approx 1$) nanopowders from silicon

vaporisation on a ZrO_2 pellet. XPS and photoluminescence characterization. Sol Energy 78:763–771
49. Wang PW, Bater S, Zhang LP, Ascherl M, Craig JH Jr (1995) XPS investigation of electron beam effects on a trimethylsilane dosed Si(100) surface. Appl Surf Sci 90:413–417
50. Moulder JF, Stickle WF, Sobol PE, Bomben KD (1992) Handbook of X-ray photoelectron spectroscopy. Perkin-Elmer Corporation, Physical Electronic Division, Eden Prairie
51. Contarini S, Howlett SP, Rizzo C, De Angelis BA (1991) XPS study on the dispersion of carbon additives in silicon carbide powders. Appl Surf Sci 51:177–183
52. Smith KL, Black KM (1984) Characterization of the treated surfaces of silicon alloyed pyrolytic carbon and SiC. J Vac Sci Technol A 2:744–747
53. Beverskog B, Puigdomenech I (1997) Revised Pourbaix diagrams for copper at 25 to 300°C. J Electrochem Soc 144:3476–3483
54. Alfantazi AM, Ahmed TM, Tromans D (2009) Corrosion behavior of copper alloys in chloride media. Mater Des 30:2425–2430
55. Pourbaix M (1974) Atlas of electrochemical equilibria in aqueous solutions, 2nd edn. NACE International, Houston
56. Keil P, Lützenkirchen-Hecht D, Frahm R (2007) Investigation of room temperature oxidation of Cu in air by Yoneda-XAFS. AIP Conf Proc 882:490–492
57. Vainshtein JS, Yeltsina OS, Terukov EI, Sreseli OM (2013) Photocurrent and photovoltage spectroscopy of amorphous silicon nanoclusters. Physica E 49:72–75
58. Kurokawa Y, Yamada S, Konagai M (2012) Numerical approach to the performance of silicon quantum dots superlattice solar cells taking into account the quantum effect. Jpn J Appl Phys 51:10NE09
59. Gallis S, Nikas V, Huang M, Eisenbraun E, Kaloyeros AE (2007) Comparative study of the effects of thermal treatment on the optical properties of hydrogenated amorphous silicon-oxycarbide. J Appl Phys 102:024302
60. Narisawa M, Kawai T, Watase S, Matsukawa K, Dohmaru T, Okamura K, Iwase A (2012) Long-lived photoluminescence in amorphous Si–O–C(–H) ceramics derived from polysiloxanes. J Am Ceram Soc 95:3935–3940
61. Shevchuk SL, Maishev YP (2005) Silicon oxycarbide thin films deposited from viniltrimethoxysilane ion beams. Thin Solid Films 492:114–117
62. Nakano Y, Saeki S, Morikawa T (2009) Optical bandgap widening of P-type Cu_2O films by nitrogen doping. Appl Phys Lett 94:022111
63. Kumar V, Masudy-Panah S, Tan CC, Wong TKS, Chi DZ, Dalapati GK (2013) Copper oxide based low cost thin film solar cells. In: 2013 IEEE 5th international nanoelectronics conference (INEC), pp 443–445. doi: 10.1109/INEC.2013.6466072
64. Zhang X, Kostecki R, Richardson TJ, Pugh JK, Ross PN Jr (2001) Electrochemical and infrared studies of the reduction of organic carbonates. J Electrochem Soc 148:A1341–A1345
65. Baxter I, Cother LD, Dupuy C, Lickiss PD, White AJP, Williams DJ (1997) Hydrogen bonding to silanols. In: ECTOC-3 (Electronic Conference on Trends in Organometallic Chemistry). http://www.ch.ic.ac.uk/ectoc/ectoc-3/
66. Smirnov V, Lambertz A, Finger F (2015) Electronic and structural properties of N-Type microcrystalline silicon oxide (Mc-Sio_x:H) films for applications in thin film silicon solar cells. Energy Procedia 84:71–77
67. Walls JM, Smith R (1994) Surface science techniques. Elsevier, Oxford
68. Cumpson PJ, Seah MP (1997) Elastic scattering corrections in AES and XPS. II. Estimating attenuation lengths and conditions required for their valid use in overlayer/substrate experiments. Surf Interface Anal 25:430–446